# $K$-shell ionization under zone-axis electron-diffraction conditions

T.W. Josefsson and L.J. Allen
*School of Physics, University of Melbourne, Parkville, Victoria 3052, Australia*

P.R. Miller and C.J. Rossouw
*Division of Materials Science and Technology, Commonwealth Scientific and Industrial Research Organization, Private Bag 33, Rosebank MDC, Clayton, Victoria 3169, Australia*

(Received 4 April 1994)

A comprehensive theoretical treatment for the inelastic scattering of fast electrons in a crystalline environment is applied to account for variations in characteristic x-ray emission rates from spinel and chromia under zone-axis diffraction conditions for 300-keV electrons. X-ray counts as well as backscattered-electron contrast are recorded as the beam is tilted by about 70 mrad on a two-dimensional scan raster. Calculated $K$-shell ionization and backscattering cross sections, based on a model which takes into account interaction delocalization, thermal diffuse scattering, and the consequent thickness-dependent channeling effects in a realistic way, are in good agreement with experiment.

## I. INTRODUCTION

In this paper an extensive theoretical and experimental study is made of the variation in characteristic x-ray yields from spinel ($MgAl_2O_4$) and chromia ($Cr_2O_3$) under dynamical zone-axis diffraction conditions. This extends the systematic row diffraction studies on spinel in earlier work[1] in that localization effects appear more strongly when the dynamical fast electron wave function is subject to two-dimensional fluctuations as a function of thickness and orientation. Zone-axis x-ray emission maps have previously been obtained by Bielicki[2] and by Christenson and Eades,[3] who have investigated associated experimental issues.[4–6] Correspondence between x-ray emission maps and backscattered-electron (BSE) contrast was observed in the early work of Duncumb.[7] In this work, BSE contrast has been acquired simultaneously with the x-ray counts, where the counts are recorded as a function of incident beam tilt near the symmetrical zone-axis orientation. A fuller discussion on the theory of BSE contrast used here is presented elsewhere.[8] The theory presented by Allen and Rossouw[9,10] incorporating full ionization kinematics and delocalization of the interaction from first principles, is employed to calculate the $(e,2e)$ ionization cross sections. This model significantly enhances earlier work by Taftø.[11] Ionization by dechanneled electrons which have undergone thermal diffuse scattering[12–15] (TDS) and further delocalization of the ionization interaction due to thermal fluctuations of target atoms are also incorporated.[10] Appropriate integration over final states of the (undetected) scattered fast electron, as well as the ejected target electron, is performed for the ionization events.[16–18] Calculated variations in both x-ray count rate and BSE contrast with incident beam orientation are shown to be in good agreement with experiment.

Effects of delocalization on the orientation dependence of x-ray yields has ramifications in standard atom location by channeling enhanced microanalysis (ALCHEMI) using the ratio method,[19,20] and various methods have been proposed to account for delocalization.[21] The statistical ALCHEMI approach[20] has been shown to be less sensitive to delocalization effects. The significance of full $(e,2e)$ scattering kinematics in describing the delocalization of inner shell ionization events is addressed in this paper. The use of light elements, such as oxygen, as reference sites has until recently been difficult but considerably extends the range and applicability of ALCHEMI to oxides. The first experimental observation of a dynamical channeling effect in oxygen $K$-shell x-ray emission was reported by Qian *et al.*[22] (also from the spinel $MgAl_2O_4$), in the systematic row orientation. Allen *et al.*[1] have recently confirmed these results and, in particular, considered a theoretical model for $(e,2e)$ ionization in a crystalline environment[9,10,23] that, contrary to previous simpler models, describes the observed channeling effects quantitatively.

## II. THEORY

The wave function of the fast incident electron in the crystal, taking inelastic scattering resulting in absorption into account, may be described as a linear superposition of Bloch states with complex wave vectors $\mathbf{K}+\lambda^i\hat{\mathbf{n}}$, such that[13]

$$\psi(\mathbf{K},\mathbf{r}) = \sum_i \alpha^i \sum_{\mathbf{g}} C^i_{\mathbf{g}} \exp[i(\mathbf{K}+\lambda^i\hat{\mathbf{n}}+\mathbf{g})\cdot\mathbf{r}] , \quad (1)$$

where the wave vector $\mathbf{K}$ in the crystal is corrected for refraction and the unit vector $\hat{\mathbf{n}}$ is an inwardly directed surface normal. Here $\alpha^i$ is the excitation amplitude of the $i$th Bloch state, and the Bloch state coefficients $C^i_{\mathbf{g}}$ (the index $\mathbf{g}$ refers to the reciprocal lattice vectors $\mathbf{g}$) are

 

components of the eigenvector corresponding to a complex eigenvalue $\lambda^i = \gamma^i + i\eta^i$. The real part of the eigenvalue $\gamma^i$ maps out the elastic dispersion surface, and the imaginary part $\eta^i$ is the absorption coefficient, resulting from inelastic scattering. The wave function is obtained through solution of the standard dynamical scattering equations of Bethe,

$$[\mathrm{K}^2 - (\mathbf{K} + \lambda^i \hat{\mathbf{n}} + \mathbf{g})^2] C^i_{\mathbf{g}} + \sum_{\mathbf{h}} U_{\mathbf{g},\mathbf{h}} C^i_{\mathbf{h}} = 0 \,, \qquad (2)$$

generalized to include inelastic scattering,[24] such that the complex (in general non-Hermitian) scattering potential matrix $U_{\mathbf{g},\mathbf{h}}$ has elements expressed as the sum of elastic $U^{\mathrm{el}}_{\mathbf{g},\mathbf{h}}$ and nonlocal inelastic $U^{\mathrm{inel}}_{\mathbf{g},\mathbf{h}}$ scattering potential coefficients, $U_{\mathbf{g},\mathbf{h}} = U^{\mathrm{el}}_{\mathbf{g},\mathbf{h}} + iU^{\mathrm{inel}}_{\mathbf{g},\mathbf{h}}$.

We now specifically consider the case of electron impact ionization. The contribution to the total inelastic scattering potential coefficients $U^{\mathrm{inel}}_{\mathbf{g},\mathbf{h}}$, due to ionization in the crystal lattice (denoted by $U^{\mathrm{ion}}_{\mathbf{g},\mathbf{h}}$), are given by,[9]

$$U^{\mathrm{ion}}_{\mathbf{g},\mathbf{h}} = \frac{1}{V_c} \sum_n \exp[i(\mathbf{h}-\mathbf{g})\cdot \boldsymbol{\tau}_{\beta_n}] \times \exp[-M(\mathbf{g}-\mathbf{h})] f^{\mathrm{ion}}_{\beta}(\mathbf{g},\mathbf{h}) \,, \qquad (3)$$

where $\boldsymbol{\tau}_{\beta_n}$ are the $n$ lattice sites of the atom of species $\beta$ in the unit cell, $M(\mathbf{q}) = 1/2\mathrm{q}^2\langle u^2_\beta\rangle$ is the Debye-Waller factor for the atom of species $\beta$, and $V_c$ is the unit cell volume. The ionization kinematics term (the so-called atomic ionization form factor) is defined by

$$f^{\mathrm{ion}}_{\beta}(\mathbf{g},\mathbf{h}) = \frac{4n}{(2\pi)^3 a_0^{*2}} \int_0^{\kappa_{\max}} k' \kappa^2 d\kappa \int \frac{1}{Q^2_{\mathbf{g}} Q^2_{\mathbf{h}}} d\Omega_{k'} \times \int F(\mathbf{Q}_{\mathbf{g}},\boldsymbol{\kappa}) F^*(\mathbf{Q}_{\mathbf{h}},\boldsymbol{\kappa}) d\Omega_{\kappa} \,. \qquad (4)$$

The "momentum" transfer $\mathbf{q}$ is defined in terms of the incident and scattered wave vectors $\mathbf{k}$ and $\mathbf{k}'$ by $\mathbf{q} = \mathbf{k} - \mathbf{k}'$. Furthermore, $\boldsymbol{\kappa}$ is the ejected electron wave vector, $n$ is the number of electrons in the target shell (i.e., $n$=2 for $K$-shell ionization), $a_0^*$ is the relativistic Bohr radius, and $\mathbf{Q}_{\mathbf{g}} = \mathbf{q} + \mathbf{g}$. The transition matrix elements

$$F(\mathbf{q},\boldsymbol{\kappa}) = \int u^*_f(\boldsymbol{\kappa},\mathbf{r}') \exp\, i(\mathbf{q}\cdot\mathbf{r}') u_i(\mathbf{r}') d\mathbf{r}' \qquad (5)$$

are obtained between a discrete initial and an orthogonalized continuum final state. The use of a screened hydrogenic model[25,26] for the tightly bound initial $K$-shell state, and an orthogonal continuum final state, is necessary for realistic interaction localization and kinematics. The details of the calculation of the $U^{\mathrm{ion}}_{\mathbf{g},\mathbf{h}}$ are discussed elsewhere[10] and will not be repeated here.

The rate of characteristic x-ray emission is proportional to the primary production of inner shell holes. The primary ionization cross section $\sigma$ is sensitive to the nature of the incident electron wave function, which in a crystal may be severely distorted from a plane wave form. This is particularly the case for zone-axis diffraction conditions. In a simple form, the cross section for inelastic scattering can be given as

$$\sigma = \frac{2m}{\hbar^2 k} \int |\psi(\mathbf{r})|^2 V_I(\mathbf{r}) d\mathbf{r} \,, \qquad (6)$$

where the integration is over the whole crystal volume and $V_I(\mathbf{r})$ represents the inelastic scattering potential.[27] A contribution to $\sigma$ from the diffuse background should also be taken into account.[28] Using a Bloch wave model for propagation of the fast electron in the crystal, $\sigma$ may be written[1,10] as

$$\sigma = NV_c \left\{ \left[ 1 - \sum_{ij} B^{ij}(t) \sum_{\mathbf{g}} C^i_{\mathbf{g}} C^{j*}_{\mathbf{g}} \right] \mu_{0,0} + \sum_{ij} B^{ij}(t) \sum_{\mathbf{g},\mathbf{h}} C^i_{\mathbf{g}} C^{j*}_{\mathbf{h}} \mu_{\mathbf{h},\mathbf{g}} \right\} \,, \qquad (7)$$

where $N$ is the number of unit cells (exposed to electron flux) in the crystal. The $B^{ij}(t)$ are given by[1,10]

$$B^{ij}(t) = \alpha^i \alpha^{j*} \frac{\exp[i(\lambda^i - \lambda^{j*})t] - 1}{i(\lambda^i - \lambda^{j*})t} \,, \qquad (8)$$

where $t$ is the specimen thickness. The terms $\mu_{\mathbf{h},\mathbf{g}}$ are related to the nonlocal inelastic ionization potential coefficients $U^{\mathrm{ion}}_{\mathbf{h},\mathbf{g}}$, by $\mu_{\mathbf{h},\mathbf{g}} = U^{\mathrm{ion}}_{\mathbf{h},\mathbf{g}}/k$. It is important to note that while the $\mu_{\mathbf{h},\mathbf{g}}$ refer to ionization only, the scattering coefficients $\lambda^i$ and the Bloch state coefficients $C^i_{\mathbf{g}}$ in Eq. (7) and Eq. (8) come from solutions to the total scattering equations [cf. Eq. (2)], and hence include all forms of inelastic scattering. In particular, the inclusion of TDS is crucially important[1] to obtain accurate ionization cross sections.

Although TDS leads to the formation of Kikuchi bands, reflecting the dynamical nature of the scattered fast electron, when integrated over all possible scattering angles the contribution of these incoherent TDS electrons to $\sigma$ in effect averages to a kinematic (plane wave) term. The first term in Eq. (7) (the factor in square brackets multiplied by $\mu_{0,0}$) accounts for ionization by such incoherent electrons. That is to say, ionization by electrons that have been "dechanneled" from the dynamical elastic beams, by wide angle (mostly TDS) scattering. The second term containing $\mu_{\mathbf{h},\mathbf{g}}$ represents a dynamical contribution to $\sigma$ that is also attenuated by inelastic scattering such as TDS. In the limit as the scattering becomes purely kinematic, as is the case for polycrystalline solids, or as the thickness $t \to \infty$, Eq. (7) reduces to $\sigma = NV_c\mu_{0,0}$, the usual kinematic result.

The cross section expression of Eq. (7) is easily adapted for other inelastic interactions. The terms $B^{ij}(t)$ and the Bloch wave coefficients $C^i_{\mathbf{g}}$ represent the dynamics of the electron propagation through the crystal. All elastic and inelastic scattering (resulting in absorption effects) influences the dynamics, and are necessarily included through the eigenvalues $\lambda^i$ in $B^{ij}(t)$. It is the $\mu_{\mathbf{h},\mathbf{g}}$ that represent a particular inelastic scattering process (occurring against the background of the other inelastic processes), and that define the interaction kinematics for

this particular process. The cross section for any inelastic scattering process may be calculated from Eq. (7), given the appropriate $\mu_{\mathbf{h},\mathbf{g}}$ for that interaction. We note that the interaction between different Bloch states is included in Eq. (7). This is crucial for a detailed description of the scattering (particularly for thin crystals), although in some circumstances (such as for thick crystals), an independent Bloch state model may suffice.[29]

In the BSE calculations of Rossouw *et al.*[8] the $\mu_{\mathbf{h},\mathbf{g}}$ for the large angle, large momentum transfer BSE process is calculated, as for the TDS used throughout this work, in the Einstein model.[13] We may write an expression similar to Eq. (3) for the inelastic BSE potential coefficients $U^{\mathrm{BSE}}_{\mathbf{g},\mathbf{h}}$, in terms of the inelastic BSE form factors $f^{\mathrm{BSE}}_{\beta}(\mathbf{g},\mathbf{h})$,

$$U^{\mathrm{BSE}}_{\mathbf{g},\mathbf{h}} = \frac{1}{V_c}\sum_{\beta n}\exp[i(\mathbf{h}-\mathbf{g})\cdot\boldsymbol{\tau}_{\beta_n}]f^{\mathrm{BSE}}_{\beta}(\mathbf{g},\mathbf{h})\,. \quad (9)$$

The summation is now over all atom sites and all the atom species in the unit cell. The Debye-Waller factor in Eq. (3) is implicit in the definition of the BSE form factor and hence excluded in Eq. (9). The BSE form factor is defined[8] as

$$f^{\mathrm{BSE}}_{\beta}(\mathbf{g},\mathbf{h}) = k\int_0^{2\pi} d\phi \int_{\theta_{\min}}^{\theta_{\max}} \sin\theta d\theta f_{\beta}(\mathbf{q}+\mathbf{g})f_{\beta}(\mathbf{q}+\mathbf{h})\{\exp[-M(\mathbf{g}-\mathbf{h})] - \exp[-M(\mathbf{q}+\mathbf{g}) - M(\mathbf{q}+\mathbf{h})]\}\,, \quad (10)$$

where $f_{\beta}(\mathbf{q})$ is the usual elastic scattering form factor, and the region of integration over the scattered electron solid angle $d\Omega_{k'} = \sin\theta d\theta d\phi$ in Eq. (10) is such that the polar angle $\theta$ is restricted to lie in the range ($\theta_{\min}$ to $\theta_{\max}$) of the backscattered-electron detector.[8] The BSE cross section may be calculated using Eq. (7) as for the ionization cross section.

## III. EXPERIMENTAL DETAILS

A Gatan double-tilt liquid-nitrogen-cooled stage was used at 110 K in a Philips CM30 transmission electron microscope (TEM) in rocking beam mode with a 30 $\mu$m condenser aperture (convergence semiangle of 0.9 mrad) and accelerating voltage measured[30] to be 302.75 keV.

The rocking beam facility was externally controlled using an AT computer in conjunction with the CM30 remote control software package. The beam may be rocked two dimensionally through up to 70 mrad with preset number of pixels in orthogonal $x$ and $y$ scan directions and preset acquisition time. Maps from up to four x-ray windows defined in the energy dispersive x-ray analysis (EDX) PV9900 software and from up to two analog signals selected from bright field, annular dark field, or BSE detectors can be recorded simultaneously. Acquisition can be paused at the end of each $x$ scan in case specimen translation correction is necessary. A beam of 0.2 $\mu$m diameter was located onto areas of reasonably uniform thickness and orientation, and the beam rocked two dimensionally through about 70 mrad. Typically the two-dimensional angular scan would involve about 80 × 60 pixels, and with 1 s/pixel integration time each set of maps may take up to 2 h to record. This requires a high degree of beam current and specimen stage stability. Beam current was measured before and after the experiment and was found to change by less than 5%. Specimen stability was monitored during the course of the experiment, but translation corrections were avoided

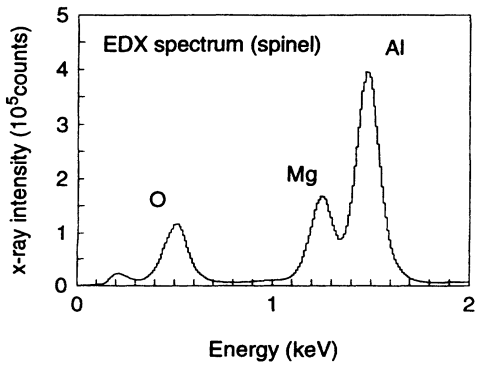


FIG. 1. EDX spectrum for spinel obtained over the total acquisition time, showing the Al, Mg, and O peaks.

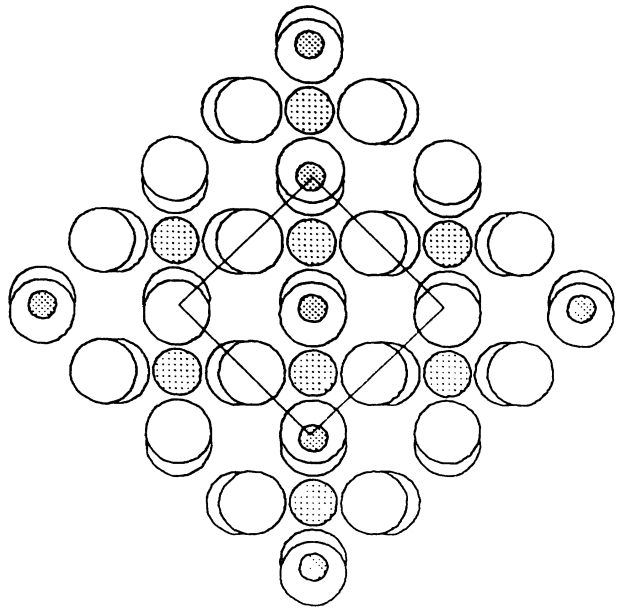

FIG. 2. The projected (along ⟨001⟩) atomic lattice sites for spinel. The Al atoms (small shaded circles) project onto the O (large white circles) sites, which are in turn slightly offset. The Mg atoms (medium shaded circles) project between the Al and O sites. The box indicates the region of the unit cell over which the real-space potentials are plotted in Fig. 5 and Fig. 7.

TABLE I. Thermal mean-square-displacement parameters (at 110 K) for the constituent atoms of spinel and chromia, used to calculate the Debye-Waller factors.

| | Spinel | | | Chromia | |
|---|---|---|---|---|---|
| | Al | Mg | O | Cr | O |
| $\langle u^2 \rangle$ ($10^{-2}$ Å) | 4.012 | 3.823 | 5.658 | 5.20 | 9.30 |

TABLE II. The input parameters for spinel and chromia used in this work: $a_c$, the unit cell parameter; $E_0$, incident energy; $T$, temperature; MFP, an inelastic mean free path additional to TDS; and $t$, the crystal thickness.

| | $a_c$ | $E_0$ (keV) | $T$ (K) | MFP (Å) | $t$ (Å) |
|---|---|---|---|---|---|
| Spinel | 8.08 | 302.75 | 110 | 1400 | 2750 |
| Chromia | 5.35 | 302.75 | 110 | 1400 | 1660 |

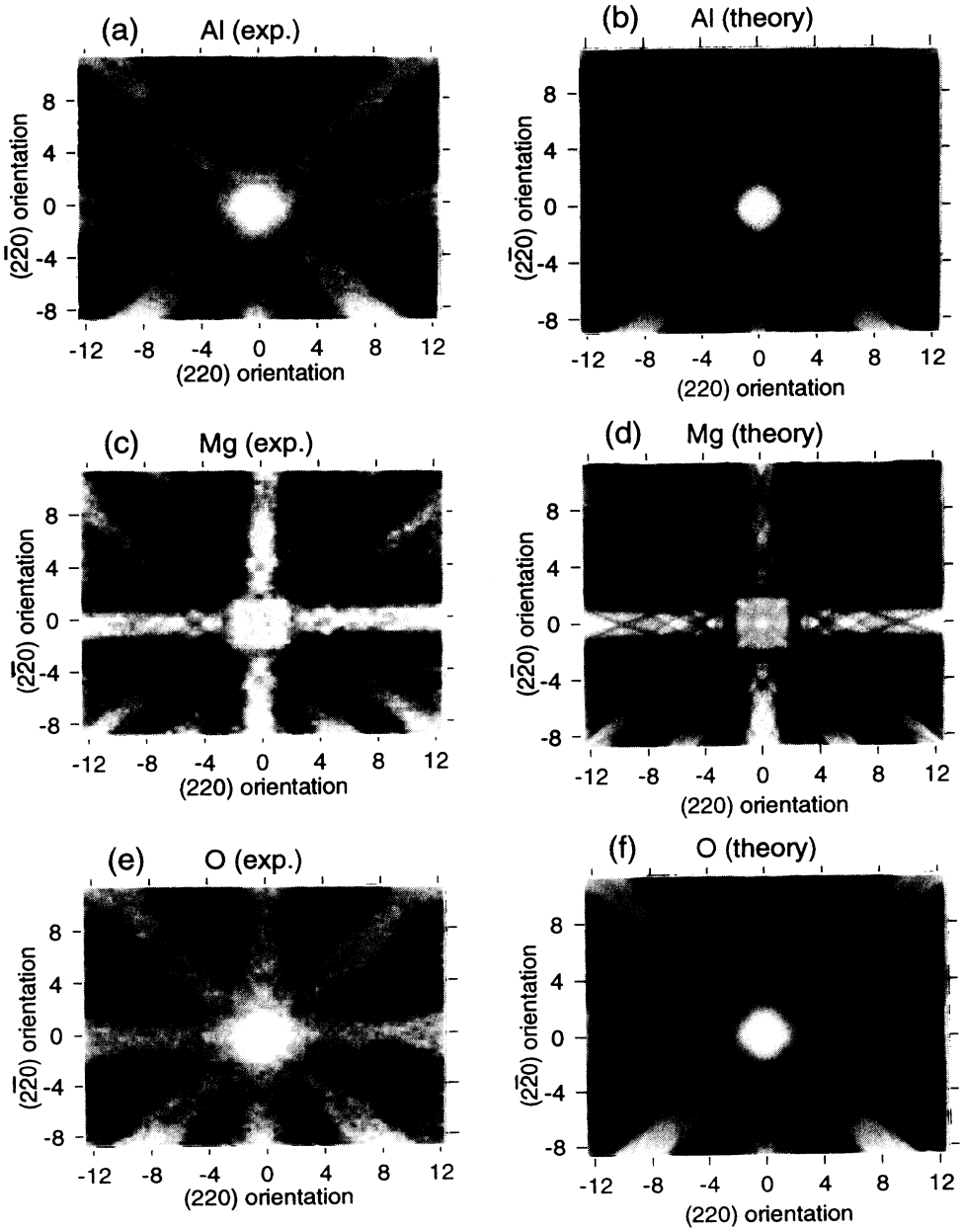


FIG. 3. The $K$-shell ionization cross sections for the constituent atoms of spinel, as a function of orientation of the incident beam near the ⟨001⟩ zone axis. The $x$ and $y$ coordinates are in units of the reciprocal lattice vectors (220) and (2$\bar{2}$0) respectively. The point (0,0) corresponds to the exact zone axis. (a) Al, experiment; (b) Al, theory; (c) Mg, experiment; (d) Mg, theory; (e) O, experiment; (f) O, theory.

TABLE III. Kinematic values of the $K$-shell ionization cross section per atom, for the constituent atoms of spinel and chromia calculated in this work.

| | Al | Mg | O | Cr |
|---|---|---|---|---|
| $\sigma$ ($10^{-5}$ Å$^2$) | 1.89 | 2.33 | 6.82 | 0.369 |

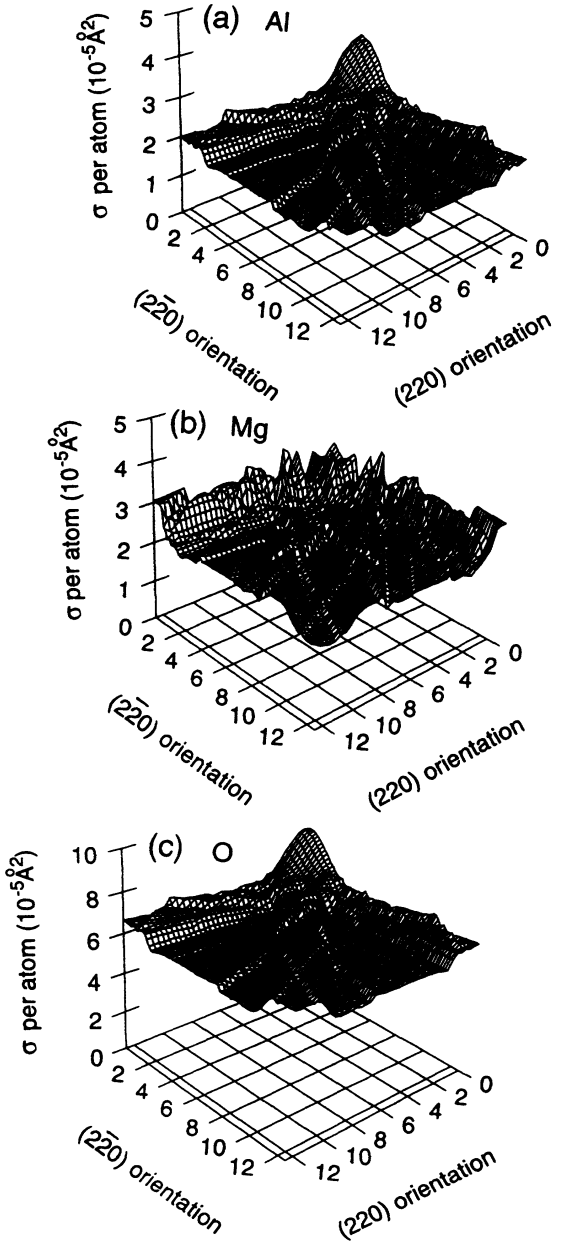


FIG. 4. The calculated $K$-shell ionization cross sections per atom as a surface plot, for the constituent atoms of spinel: (a) Al, (b) Mg, and (c) O. For clarity, only the "first quadrant" of the grey-scale scans in Fig. 3 are shown here.

if at all possible. Spherical aberration caused the beam to move slightly during rocking, resulting in some contrast changes with thickness and distortion due to changes in orientation.

## IV. CROSS SECTION CALCULATION

In order to solve the dynamical equations for the electron beam in the solid, Eq. (2), we require the elastic and inelastic scattering potential coefficients. The elastic potential is calculated in the standard way for high energy electrons, from the Doyle-Turner[31] x-ray scattering form factors converted to electron scattering form factors for neutral atoms via the Mott formula. In this high energy regime, the most significant large angle inelastic scattering process, resulting in dechanneling of the elastic beam, is TDS.[27] Due to its highly localized nature, thermal diffuse scattering is overwhelmingly the dominant process (by several orders of magnitude even at a temperature of 110 K) contributing to the off-diagonal inelastic potential coefficients $U^{\text{inel}}_{\mathbf{g},\mathbf{h}}$. Inelastic processes such as interband electronic excitations and plasmon scattering are highly delocalized and hence largely contribute only to a mean attenuation (or $U^{\text{inel}}_{0,0}$) of the incident beam.[32,33] The TDS form factors are calculated in the Einstein model, and although neglecting coherent (phonon) effects,[34] this gives good results. The ionization form factors required to calculate the $\mu_{\mathbf{h},\mathbf{g}}$ for the cross section are based on a screened hydrogenic model (an excellent approximation for the $K$-shell state) and an orthogonal modified continuum state.[25,26] The numerical evaluation technique is described elsewhere.[10] The BSE scattering matrix $\mu_{\mathbf{h},\mathbf{g}}$ is, as discussed in the previous section, based on large angle TDS scattering into an annular ring. In this case the annular ring, or window, is defined by the experimental detector as scattering through an angle of 132°–157° with respect to the incident beam.

In order to model the experimental cross section, we need to evaluate $\sigma$ from Eq. (7), as a function of incident beam direction $\mathbf{K}$, solving the dynamical scattering equations [cf. Eq. (2)] for each $\mathbf{K}$. We consider the crystal oriented so that $\mathbf{K}$ is initially in the exact zone-axis orientation, ⟨001⟩ and ⟨111⟩ for spinel and chromia, respectively. To achieve the required accuracy we have found it necessary to consider the 89 lowest $\mathbf{g}$ vectors lying in the zeroth-order Laue zone (ZOLZ). Once all the relevant inelastic scattering matrix elements $U^{\text{inel}}_{\mathbf{g},\mathbf{h}}$ lying in the ZOLZ plane have been evaluated, we solve the dynamical scattering equations at each required incident beam orientation. After evaluating the total wave function at a particular $\mathbf{K}$, in general a significantly smaller subset of Bloch states is found to have a significant excitation amplitude squared $|\alpha^i|^2$, and hence contribute appreciably to the wave function. We make use of this property in the final calculation of $\sigma$ to overcome prohibitively time consuming Bloch state and dispersion branch summations, by ordering according to $|\alpha^i|^2$ and considering only those

excited Bloch states comprising $\sim$ 99.98% of the total wave function amplitude.

## V. RESULTS AND DISCUSSIONS

### A. Spinel

The measurements were taken from an ion-beam thinned spinel sample of thickness 2750 Å [measured by convergent-beam electron-diffraction (CBED) contrast] and at a temperature of 110 K. Angular scan maps were recorded on a 79 × 58 pixel scan raster, with a recording time of 1 s/pixel. Oxygen characteristic x rays were collected within an energy window of 0.42–0.59 keV, and absolute counts varied between 519 and 777. For Mg, the energy window was 1.18–1.32 keV and the counts varied between 587 and 1166. These figures are 1.41–1.56 keV and 1347–2600 for Al. The total spectrum recorded during the mapping experiment is shown in Fig. 1, and the projection of the unit cell along the zone axis ⟨001⟩ is shown in Fig. 2. No spectral background subtraction was attempted. During mapping, the overall count rate varied between 2400 and 5500 counts/s. The BSE signal was recorded simultaneously with a relatively long time constant to reduce noise.

In Fig. 3 we show both the experimental results for the characteristic x-ray emission rates, as a function of orientation for the three elements in $MgAl_2O_4$, and the corresponding theoretical ionization cross sections, calculated from Eq. (7). Both experiment and calculated results are displayed on a logarithmic 16-level grey scale between the minimum and maximum values. The grey-scale maps span a variation in the incident beam direction of approximately 70 mrad either side of the symmetrical position at (0,0), roughly the center of the figure. The $x$ and $y$ scan coordinates are in units of ZOLZ reciprocal lattice scan vectors, (220) and $(2\bar{2}0)$, respectively, instead of degrees, to show the rapid variation in ionization rates across the Brillouin zone (BZ) boundaries. The calculated ionization cross sections are displayed as a 157 × 125 pixel grey-scale map, for the same orientations and conditions as the experiment, apart from the approximately 10% distortion in the $y$ direction of the experimental results. The Debye-Waller factors for Al, Mg, and O, pertinent to spinel at this temperature, are taken from Ref. 35, and are given here in Table I. Furthermore, following Ref. 1, an additional mean absorp-

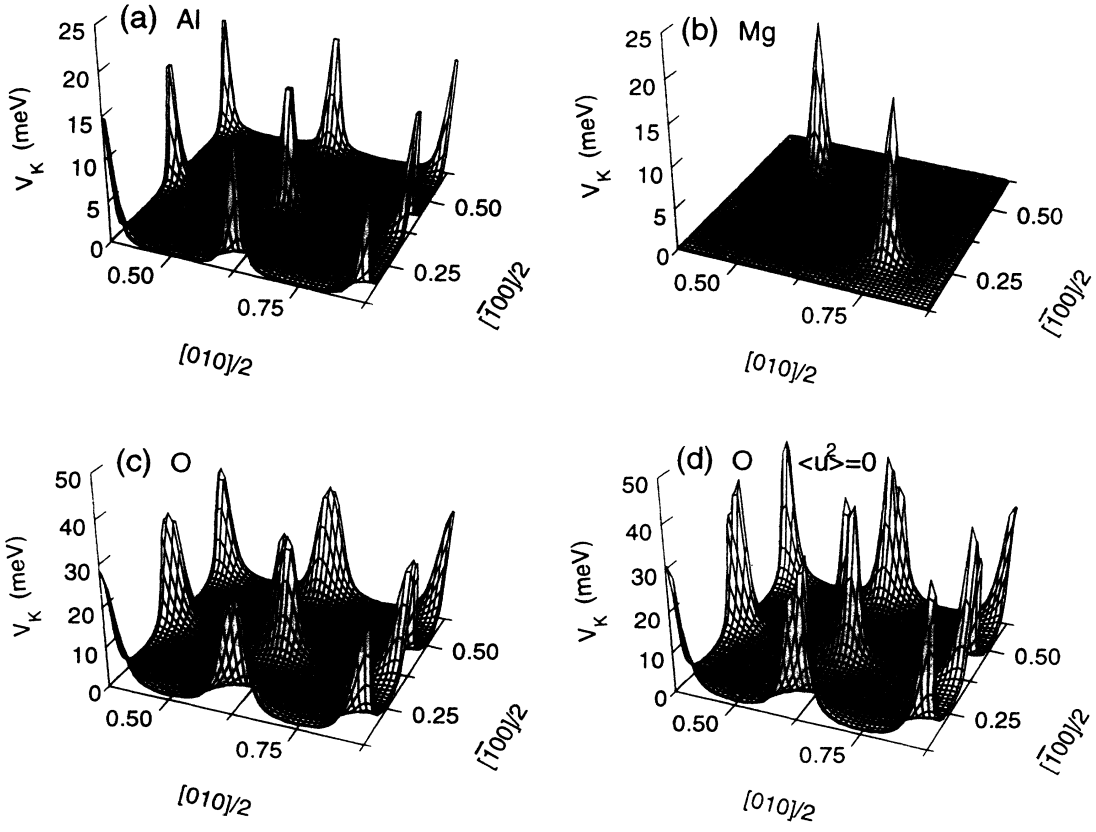


FIG. 5. The projected (along the ⟨001⟩ zone axis) equivalent local real-space ionization potentials for the constituent atoms of spinel: (a) Al, (b) Mg, (c) O, and (d) O with $\langle u^2 \rangle = 0$. The real-space scan is over the region of the unit cell indicated in Fig. 2, and is along the real-space lattice vectors [010]/2 and [$\bar{1}$00]/2.

tion with a mean free path of 1400 Å was included in the calculations, providing an overall damping of the detailed dynamical response. This is other than the mean absorption due to TDS which has a kinematic mean free path of 3600 Å, and accounts for processes other than TDS that contribute to dechanneling. The parameters used in this calculation are given in Table II, and the calculated kinematic values of the cross section are given in Table III.

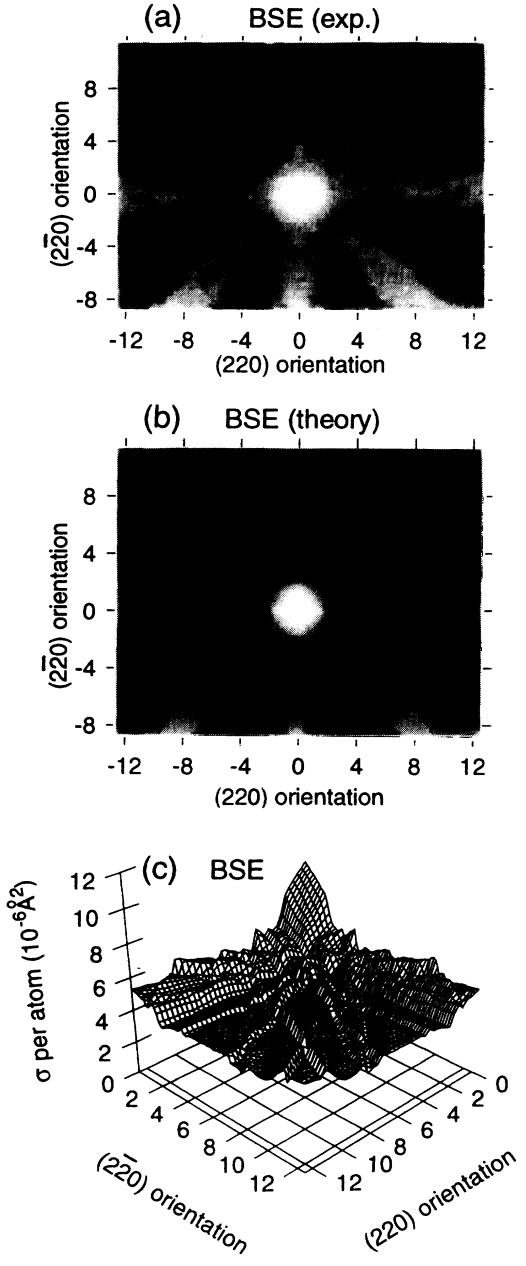


FIG. 6. The backscattered electron cross sections for spinel, as a function of incident beam orientation near the ⟨001⟩ zone axis. (a) experimental results, (b) theoretical results, (c) theoretical results (cross section per atom) on a surface plot. The point (0,0) indicates the beam is in the exact zone-axis orientation, and the $x$ and $y$ scans are in units of the reciprocal lattice vectors (220) and (2$\bar{2}$0) respectively.

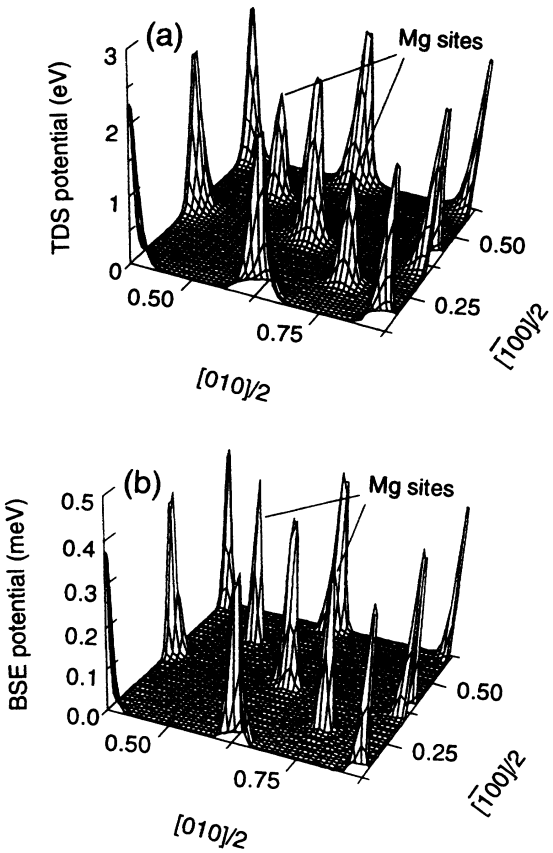


FIG. 7. The projected (along the ⟨001⟩ zone axis) equivalent local real-space potentials for (a) total thermal diffuse scattering and (b) electron backscattering, in spinel. The potentials are plotted for the region of the unit cell indicated in Fig. 2, and is along the real-space lattice vectors [010]/2 and [$\bar{1}$00]/2. The two Mg sites are marked in each figure.

The large variation observed in the ionization cross section for crystalline solids, as a function of incident angle (clearly apparent in Fig. 3), may be understood qualitatively in the Bloch wave formalism. The excitation amplitude $\alpha^i$ may change rapidly as the incident beam $\mathbf{K}$ crosses BZ boundaries.[36] This in turn, may re-

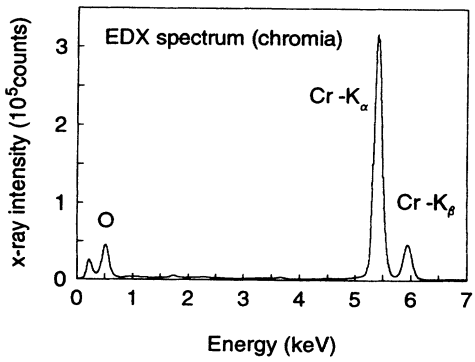


FIG. 8. EDX spectrum for chromia obtained over the total acquisition time showing the O and Cr peaks.

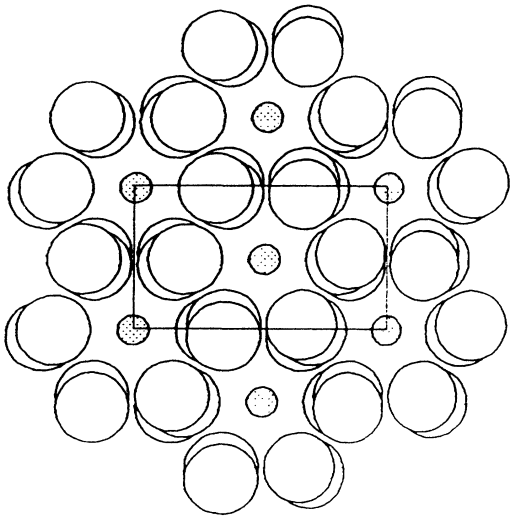

FIG. 9. The projected (along ⟨111⟩) atomic lattice sites for chromia. Several O atoms (large white circles) are seen to project onto each other with a slight offset, encircling the Cr (small shaded circles) sites. The box indicates the region of the unit cell over which the real-space potentials are plotted in Fig. 11 and Fig. 13.

sult in a rapid variation of the electron probability density in the crystal, moving selectively from one atomic site or species to another. The characteristic x-ray emission rate and ionization cross section for a particular atomic species may of course be expected to follow the electron probability density on that particular atomic species.[13,28] To understand the variation in the ionization cross section quantitatively, however, it is not sufficient to consider just the electron probability density on a particular site, but the interaction kinematics must also be taken into account.[1] This is crucial to microanalytical techniques such as ALCHEMI, where an understanding of the variation in ionization rates allows determination of both concentration and fractional site dependence of impurity atoms. The greater the localization of the interaction, the more site specific the ALCHEMI technique becomes, as has been investigated by a number of authors.[10,28,37–42] The effective interaction delocalization is particularly large for, and hence of particular significance to, light elements such as oxygen.

Al and O project onto similar positions (see Fig. 2), when viewed down ⟨001⟩, resulting in similar ionization cross section topography. For both these species there is a central "crown" with excess vertical and horizontal {220} bands, as well as excess diagonal {400} bands. For Mg, however, due to its different site symmetry, there is a deficit near the center and deficit banding along {400}. These effects, and the absolute value in the ionization cross sections per atom, can be seen more clearly in the projected surface plots of Fig. 4. For clarity, only the "first quadrant" of the grey-scale map of the ionization cross section has been displayed. The variation in the topography of the calculated cross sections about the kinematic value correlates closely with experiment. We have previously shown[1,8] that this close correspondence between theory and experiment is only reproduced by considering correct interaction delocalization and thickness-dependent dechanneling effects in the cross section.

In Fig. 5 we show projected equivalent local real-space $K$-shell ionization potentials $V_K(\mathbf{r})$, for Al, Mg, and O, in spinel. The nonlocal contribution to the ionization and backscattering interactions is relatively small, particularly at these high incident energies, and hence we consider (for the purposes of representing the real-space potential) the equivalent local approximation $U^{\text{ion}}_{\mathbf{g},\mathbf{h}} \approx U^{\text{ion}}_{\mathbf{g}-\mathbf{h},\mathbf{0}}$. The projected equivalent local real-space potentials are obtained from the summation of approximately 2000 $U^{\text{ion}}_{\mathbf{g},\mathbf{0}}$ coefficients: $V_K(\mathbf{r}) \approx \hbar^2/2m \sum_{\mathbf{g}} U^{\text{ion}}_{\mathbf{g},\mathbf{0}} \exp i(\mathbf{g}\cdot\mathbf{r})$. The projection is along the ⟨001⟩ zone axis and we have displayed the potential over one unit cell length, parallel to the real-space vectors [010]/2, and [$\bar{1}$00]/2. Comparing Fig. 5(a) with Fig. 5(c), we see the effective projected O potential is clearly more delocalized than Al. This is largely due, in effect, to the lower ionization threshold energy, but the slightly off-set projection of the O atoms (see Fig. 2) also contributes to an apparent "delocalization." The distinction between the atomic interaction delocalization and an apparent "delocalization" effect due to crystallography is clear and must not be confused. However, it is of interest to consider the thermal "broadening" effects of the Debye-Waller factor in Eq. (3). The inclusion of this term results in an additional small increase in the effective interaction "delocalization" [cf. Fig. 5(c) and Fig. 5(d)] due to thermal motion of the target atom. We see from Fig. 5(d) that the slight offset in the projected O sites (cf. Fig. 2), not present in Al, is effectively obscured in Fig. 5(c) by the presence of this Debye-Waller term.

The experimental and theoretical BSE cross sections for spinel are shown in Fig. 6. To a first-order approximation, the BSE cross section has been shown[8] to be proportional to the electron probability density on a particular site scaled by a weighted sum of the square of the atomic numbers, $Z^2_\beta$. As the BSE scattering is simply large angle TDS, it is instructive to consider a comparison with the total TDS potential. In Fig. 7 we show projected equivalent local real-space potentials, for both BSE's and the total TDS in spinel. The BSE potential, while retaining the same general form as TDS, is almost four orders of magnitude smaller and significantly more localized than the total TDS potential. The high degree of localization for BSE's is a measure of the large momentum transfer necessary for backscattering of the fast incident electron, corresponding to a significantly smaller classical impact parameter for the scattering process.[23]

### B. Chromia

The chromia sample was prepared by crushing and mounting on a holey carbon support film prior to exper-

iments at 110 K. Thickness was measured from CBED contrast to be 1660 Å. Angular maps were recorded on a 79 × 52 pixel scan raster, with a recording time of 0.7 s/pixel. Oxygen characteristic x rays were collected within an energy window of 0.4–0.55 keV, with counts varying between 51 and 134. Some overlap with the Cr $L$-shell excitations occurred, and these were mapped from a separate energy window of 0.56–0.64 keV. We have not accounted for this overlap in presentation of the O counts. Counts in this window varied between 11 and 44. The contribution from Cr $L$-shell counts was small, possibly as a result of high absorption by O in the sample and in the thin polymer window of the x-ray detector. The energy window for the Cr $K$-shell excitations was 5.25–6.07 keV and the counts varied between 532 and 1466. The total x-ray spectrum recorded during the mapping experiment is shown in Fig. 8, and the projection of the unit cell along the zone axis ⟨111⟩ is shown in Fig. 9. Again, no background subtraction was attempted, and BSE counts were recorded simultaneously with the x-ray

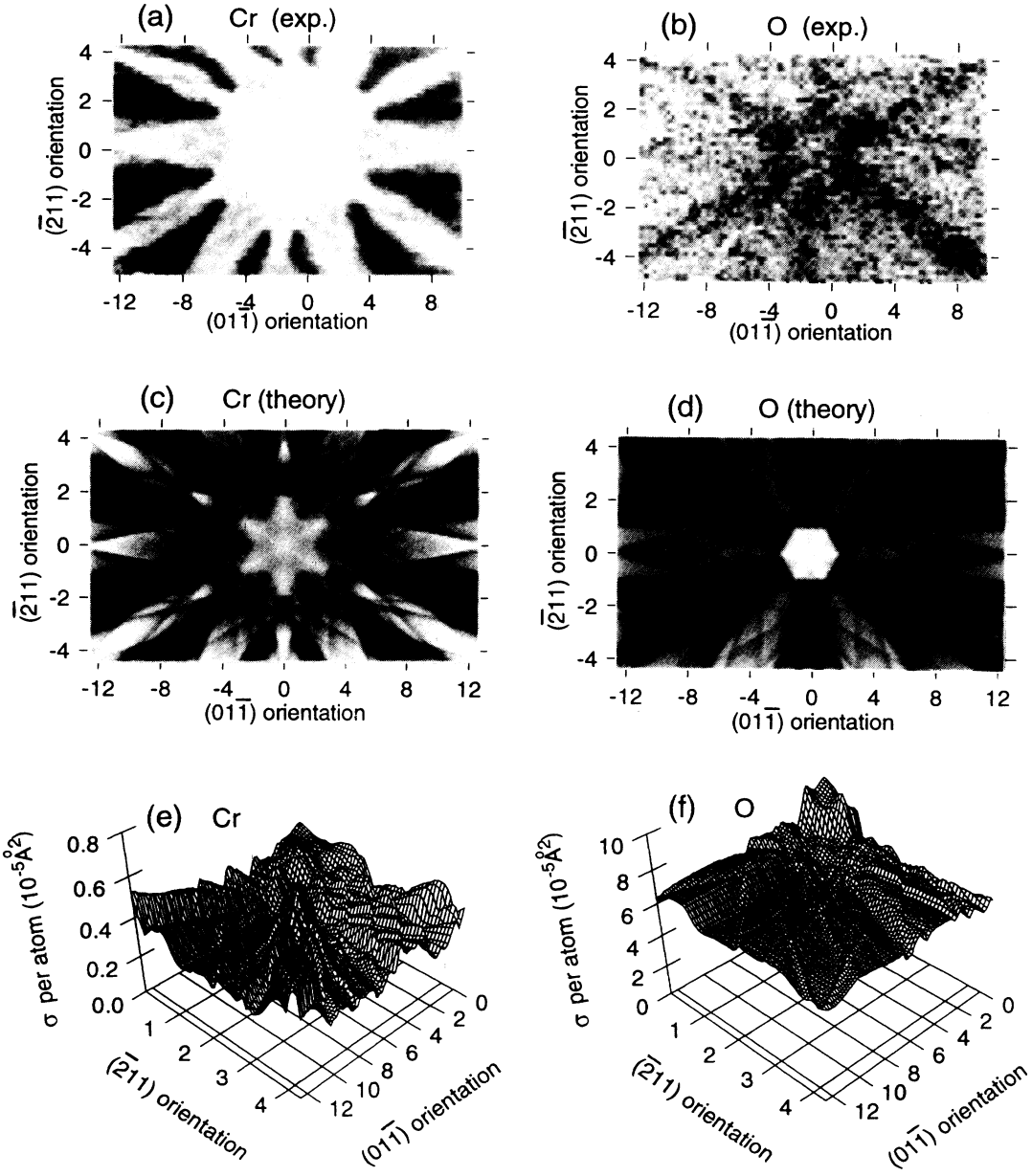


FIG. 10. The $K$-shell ionization cross sections for the constituent atoms of chromia as a function of orientation of the incident beam near the ⟨111⟩ zone axis. The $x$ and $y$ coordinates are in units of the reciprocal lattice vectors $(01\bar{1})$ and $(\bar{2}11)$ respectively, and the point (0,0) indicates the exact zone axis. (a) Cr, experiment; (b) O, experiment; (c) Cr, theory; (d) O, theory; (e) Cr, theory (cross section per atom) on a surface plot; (f) O, theory (cross section per atom) on a surface plot.

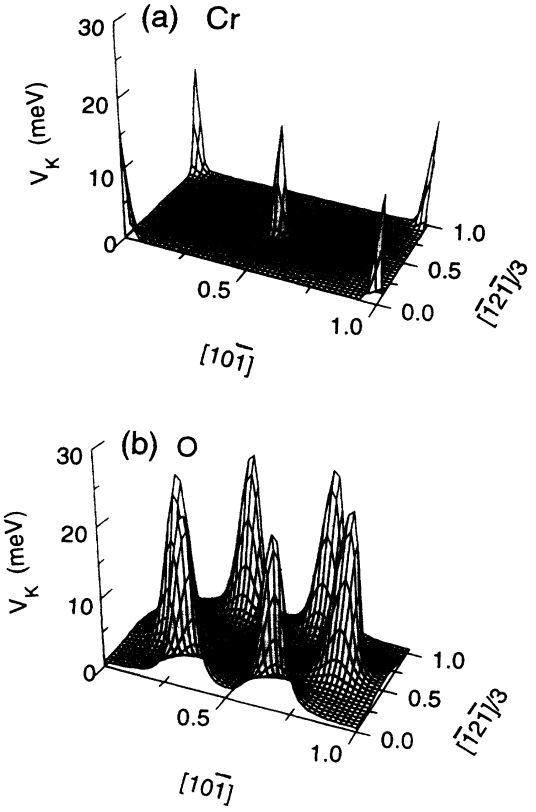


FIG. 11. The projected (along the ⟨111⟩ zone axis) equivalent local real-space ionization potentials for the constituent atoms of chromia: (a) Cr and (b) O. The real-space scan is over the region of the unit cell indicated in Fig. 9, and is along the real-space lattice vectors [10$\bar{1}$] and [$\bar{1}$2$\bar{1}$]/3.

counts.

In Fig. 10 we display the experimental and theoretical ionization cross sections for Cr and O in $Cr_2O_3$, around the ⟨111⟩ zone-axis orientation. The $x$ and $y$ scans are along (and in units of) the ZOLZ reciprocal lattice vectors, (01$\bar{1}$) and ($\bar{2}$11), respectively. The Debye-Waller factors are obtained from Ref. 34, and we have used an additional mean free path of 1400 Å in this calculation (see Table I and Table II).

In Fig. 11 we show the projected equivalent local real-space ionization potentials for Cr and O in chromia, over one unit cell along the [10$\bar{1}$] and [$\bar{1}$ 2$\bar{1}$]/3 directions. Although much of the preceding discussion for spinel applies equally to chromia, there are some significant differences. In spinel the peak effective ionization potentials for the constituent atoms are all of the same magnitude, with O only slightly more delocalized than Al or Mg. However, for chromia the projected Cr ionization potential, Fig. 11(a), is significantly more localized (although not greater in peak magnitude) than for O [Fig. 11(b)], or any of the species in spinel. This results in the ionization cross section for O being significantly more diffuse and showing far less relative change across BZ boundaries than for Cr (cf. Fig. 10). This effect was also apparent for O in spinel (Fig. 3 and Fig. 4), albeit to a lesser degree due to the similar localization of the ionization interaction for these light atoms. The ionization cross section is effectively proportional to the volume under the potential, and so it is not surprising that the Cr cross section is approximately an order of magnitude smaller than O (see Table III). We note that this effect is not seen as clearly in the calculated grey-scale ionization maps, due to the

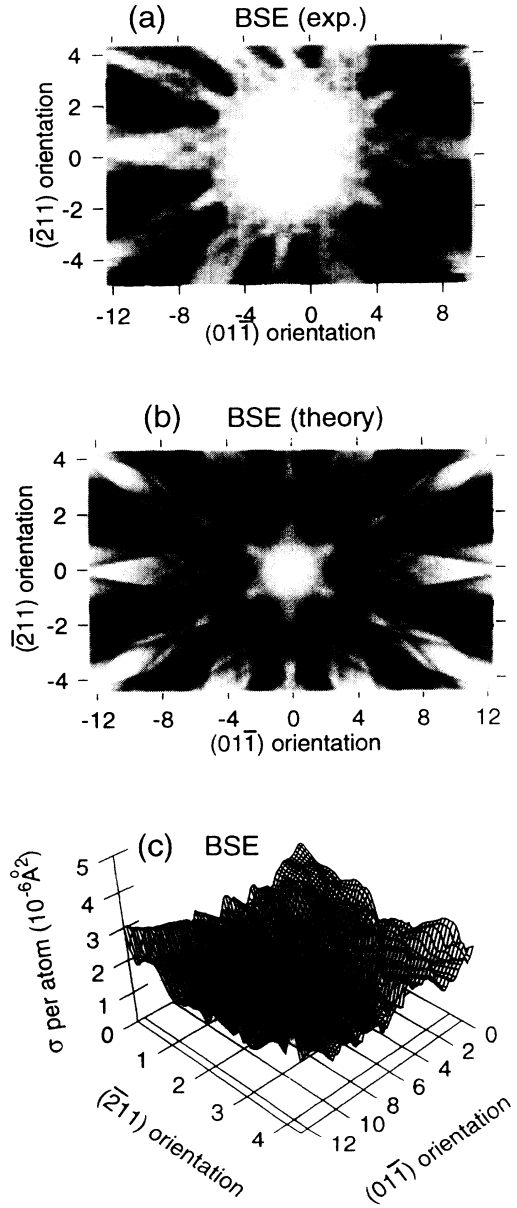


FIG. 12. The backscattered electron cross sections for chromia, as a function of incident beam orientation near the ⟨111⟩ zone axis. (a) experimental results, (b) theoretical results, (c) theoretical results (cross section per atom) as a surface plot. The point (0,0) indicates the beam is in the exact zone-axis orientation, and the $x$ and $y$ scans are in units of the reciprocal lattice vectors (01$\bar{1}$) and ($\bar{2}$11) respectively.

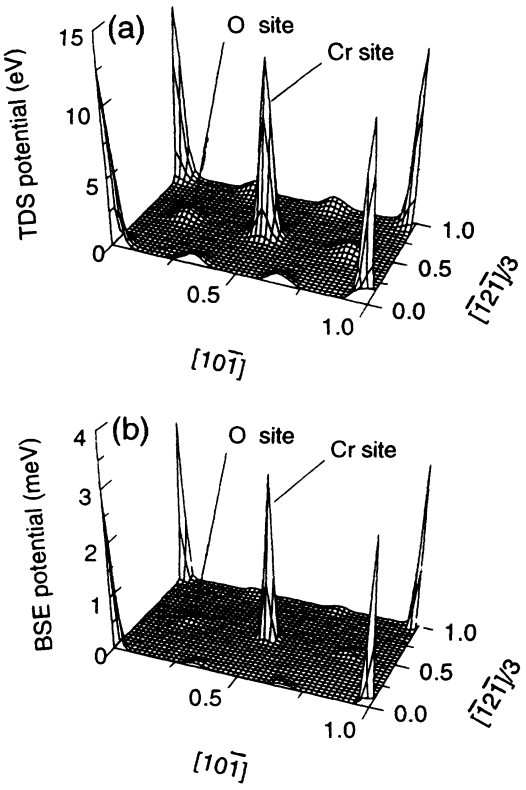


FIG. 13. The projected (along the ⟨111⟩ zone axis) equivalent local real-space potentials for (a) total thermal diffuse scattering and (b) electron backscattering, in chromia. The potentials are plotted over the region of the unit cell indicated in Fig. 9, and is along the real-space lattice vectors $[10\bar{1}]$ and $[\bar{1}2\bar{1}]/3$. The five largest peaks are due to Cr, and the six smaller peaks are due to O.

relative intensity normalization used to display details in the cross section structure.

In Fig. 12 we show the BSE results for chromia. The projected equivalent local BSE potential has a distinctly different character to that of spinel. In spinel, the contribution to the effective TDS and BSE potentials from the constituent atoms are both of similar magnitude and localization. However, the TDS and BSE potentials for chromia (see Fig. 13) indicate that the peak contribution from Cr is both an order of magnitude greater, and substantially more localized, than that due to O. This can be understood qualitatively as the Cr/O atomic number ratio is much larger ($\approx 24/8$) than for any of the elements in spinel (for instance Al/O$\approx 13/8$), where this effect is not as apparent. For BSE contrast in chromia, we therefore expect that the Cr atoms will dominate the cross section, due to the resultant larger elastic scattering form factor at these momentum transfers [$f_\beta(\mathbf{q}) \sim Z_\beta^2$ for large $\mathbf{q}$] and hence a larger TDS form factor [Eq. (10)], and indeed this is what we found in Fig. 12. Because the Cr atoms dominate the backscattering, and because the backscattering is highly dependent on the crystallography, it is not surprising that the topography of the BSE map reflects the general form of the Cr ionization cross section [cf. Fig. 12(c) and Fig. 11(e)].

## VI. CONCLUSIONS

A raster scan technique has enabled an extensive study of the effect of electron channeling in characteristic $(e, 2e)$ x-ray emission and electron backscattering for zone-axis orientations. Applied to spinel and chromia, unambiguous evidence for channeling in oxygen x-ray emission has been observed for $K$-shell ionization. The experimental results have been accurately reproduced by the theory of Allen and Rossouw,[10] for calculating inelastic electron scattering cross sections in crystalline solids. For light elements it is crucial that the atomic ionization interaction be included in a realistic manner, and that electron dechanneling from thermal diffuse scattering (appropriately thickness integrated) be considered. In addition, it is found that large angle, large momentum transfer, thermal diffuse scattering in this same model, but with appropriately calculated inelastic scattering potentials, accounts for the observed electron backscattering to a high degree of precision.

## ACKNOWLEDGMENTS

One of us (L.J.A.) acknowledges support for this work from the Australian Research Council.

[1] L.J. Allen, T.W. Josefsson, and C.J. Rossouw, Ultramicroscopy (to be published).
[2] T. A. Bielicki, in *Proceedings of the Institute of Physics Electron Microscopy and Analysis Group EMAG*, edited by P. Doig, IOP Conf. Proc. No. 68 (Institute of Physics and Physical Society, London, 1984).
[3] K.K. Christenson and J.A. Eades, in *Proceedings of the 44th Annual Meeting EMSA*, edited by G.W. Bailey (San Francisco Press, San Francisco, 1986).
[4] K.K. Christenson and J.A. Eades, Ultramicroscopy **19**, 191 (1986).
[5] K.K. Christenson and J.A. Eades, Ultramicroscopy **26**, 113 (1988).
[6] K.K. Christenson and J.A. Eades, in *Proceedings of the 47th Annual Meeting EMSA*, edited by G.W. Bailey (San Francisco Press, San Francisco, 1989).
[7] P. Duncumb, Philos. Mag. **7**, 2101 (1962).
[8] C.J. Rossouw, P.R. Miller, T.W. Josefsson, and L.J. Allen, Philos. Mag. (to be published).
[9] L.J. Allen and C.J. Rossouw, Phys. Rev. B **42**, 11644 (1990).
[10] L.J. Allen and C.J. Rossouw, Phys. Rev. B **47**, 2446 (1993).

[11] J. Taftø, Z. Naturforsch. A **34**, 452 (1979).
[12] Y.H. Ohtsuki, *Charged Beam Interactions with Solids* (Taylor & Francis, London, 1983).
[13] L.J. Allen and C.J. Rossouw, Phys. Rev. B **39**, 8313 (1989).
[14] D.M. Bird and Q.A. King, Acta Crystallogr. A **46**, 202 (1990).
[15] D.M. Bird, Acta Crystallogr. A **46**, 208 (1990).
[16] V.W. Maslen and C.J. Rossouw, Philos. Mag. A **47**, 119 (1983).
[17] V.W. Maslen and C.J. Rossouw, Philos. Mag. A **49**, 735 (1984).
[18] C.J. Rossouw and V.W. Maslen, Philos. Mag. A **49**, 743 (1984).
[19] J.C.H. Spence and J. Taftø, J. Microsc. **130**, 147 (1983).
[20] P.S. Turner, T.J. White, A.J. O'Connor, and C.J. Rossouw, J. Microsc. **162**, 369 (1990).
[21] J. Bentley, in *Proceedings of the 44th Annual Meeting EMSA*, edited by G.W. Bailey (San Francisco Press, San Francisco, 1986), pp. 704–705.
[22] W. Qian, B. Totdal, R. Hoier, and J.C.H. Spence, Ultramicroscopy **41**, 147 (1992).
[23] L.J. Allen, Ultramicroscopy **48**, 97 (1993).
[24] H. Yoshioka, J. Phys. Soc. Jpn. **12**, 618 (1957).
[25] V.W. Maslen, J. Phys. B **16**, 2065 (1983).
[26] C.J. Rossouw and V.W. Maslen, Ultramicroscopy **21**, 277 (1987).
[27] S.J. Pennycook and D.E. Jesson, Ultramicroscopy **37**, 14 (1991).
[28] D. Cherns, A. Howie, and M.H. Jacobs, Z. Naturforsch. A **28**, 565 (1973).
[29] J. Gjonnes and J. Taftø, Nucl. Instrum. Methods **132**, 141 (1976).
[30] C.J. Rossouw and P.R. Miller, Philos. Mag. B **67**, 733 (1993).
[31] P.A. Doyle and P.C. Turner, Acta Crystallogr. A **24**, 390 (1968).
[32] T.W. Josefsson and A.E. Smith, Phys. Lett. A **180**, 174 (1993).
[33] T.W. Josefsson and A.E. Smith, Phys. Rev. B (to be published).
[34] J.J. Earney, Philos. Mag. **23**, 577 (1971).
[35] T. Yamanaka, Y. Takeuchi, and M. Tokonami, Acta Crystallogr. B **40**, 96 (1984).
[36] C.J. Rossouw and J.M. Hampikian, Philos. Mag. A **67**, 849 (1993).
[37] J. Bourdillon, P.G. Self, and W.M. Stobbs, Philos. Mag. A **44**, 1335 (1981).
[38] J. Taftø, Phys. Rev. Lett. **51**, 654 (1983).
[39] F. Glas and P. Henoc, Philos. Mag. A **56**, 311 (1987).
[40] F. Glas, Ultramicroscopy **28**, 61 (1989).
[41] J. Taftø and O.L. Krivanek, Nucl. Instrum. Methods **194**, 153 (1982).
[42] Y. Nakata, T. Tadaki, and K. Shimizu, Ultramicroscopy **39**, 72 (1991).

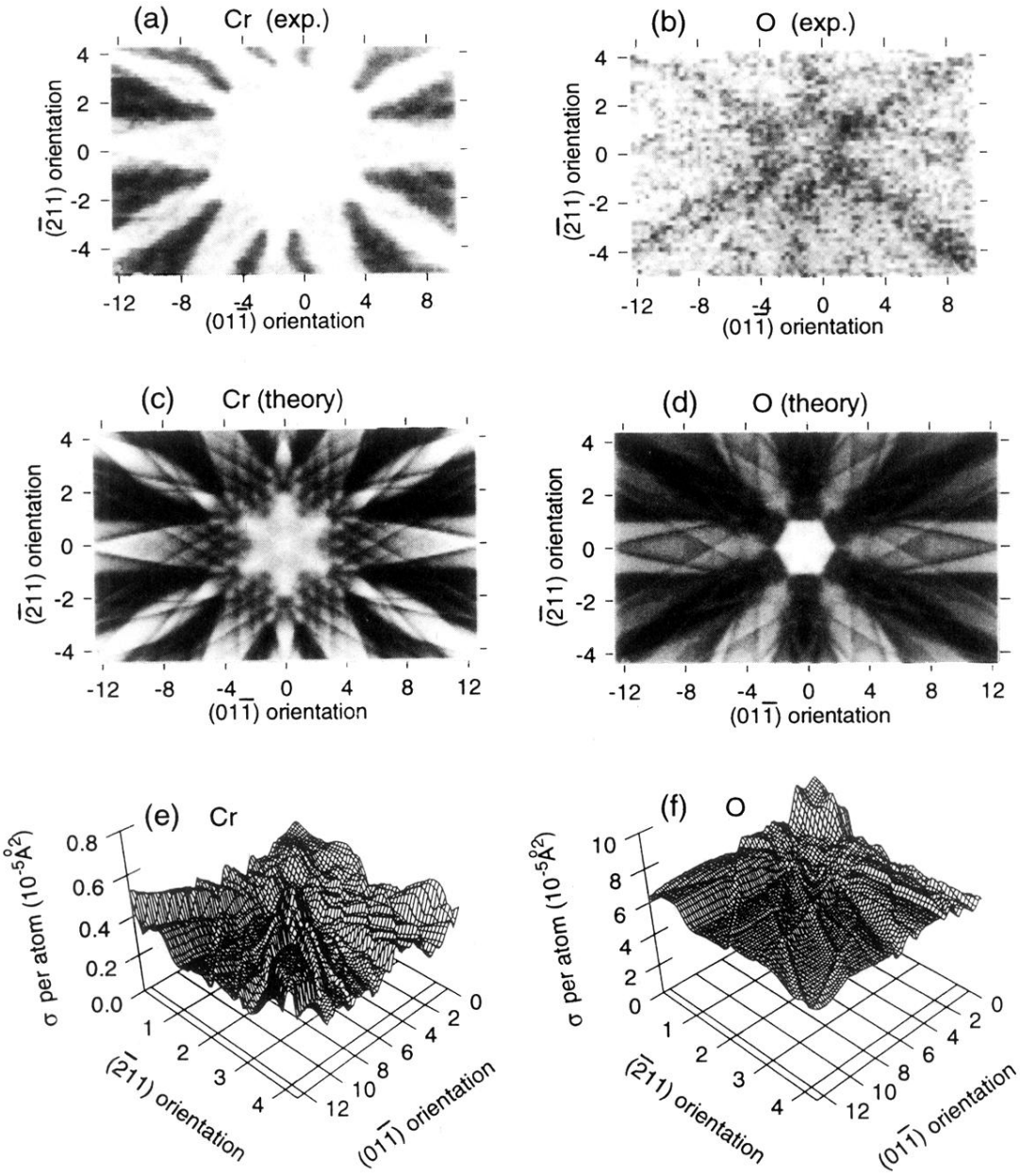


FIG. 10. The $K$-shell ionization cross sections for the constituent atoms of chromia as a function of orientation of the incident beam near the $\langle 111 \rangle$ zone axis. The $x$ and $y$ coordinates are in units of the reciprocal lattice vectors $(01\bar{1})$ and $(\bar{2}11)$ respectively, and the point (0,0) indicates the exact zone axis. (a) Cr, experiment; (b) O, experiment; (c) Cr, theory; (d) O, theory; (e) Cr, theory (cross section per atom) on a surface plot; (f) O, theory (cross section per atom) on a surface plot.

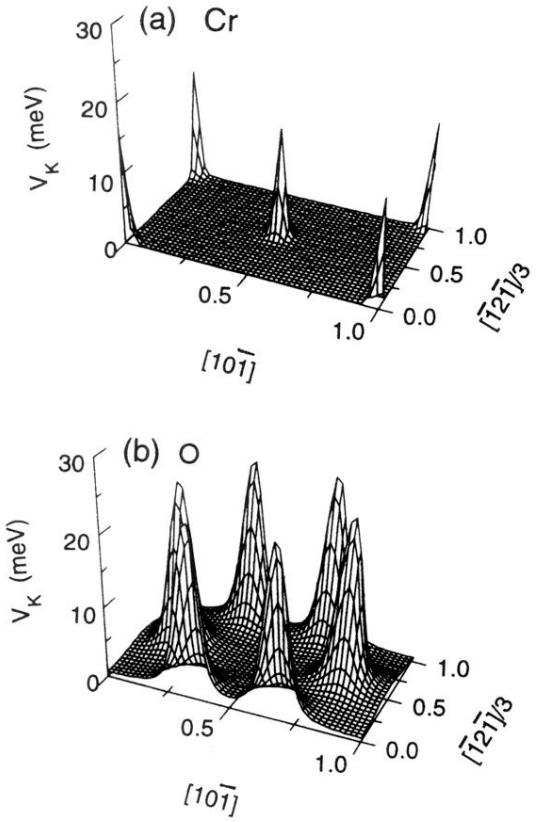


FIG. 11. The projected (along the $\langle 111 \rangle$ zone axis) equivalent local real-space ionization potentials for the constituent atoms of chromia: (a) Cr and (b) O. The real-space scan is over the region of the unit cell indicated in Fig. 9, and is along the real-space lattice vectors $[10\bar{1}]$ and $[\bar{1}2\bar{1}]/3$.

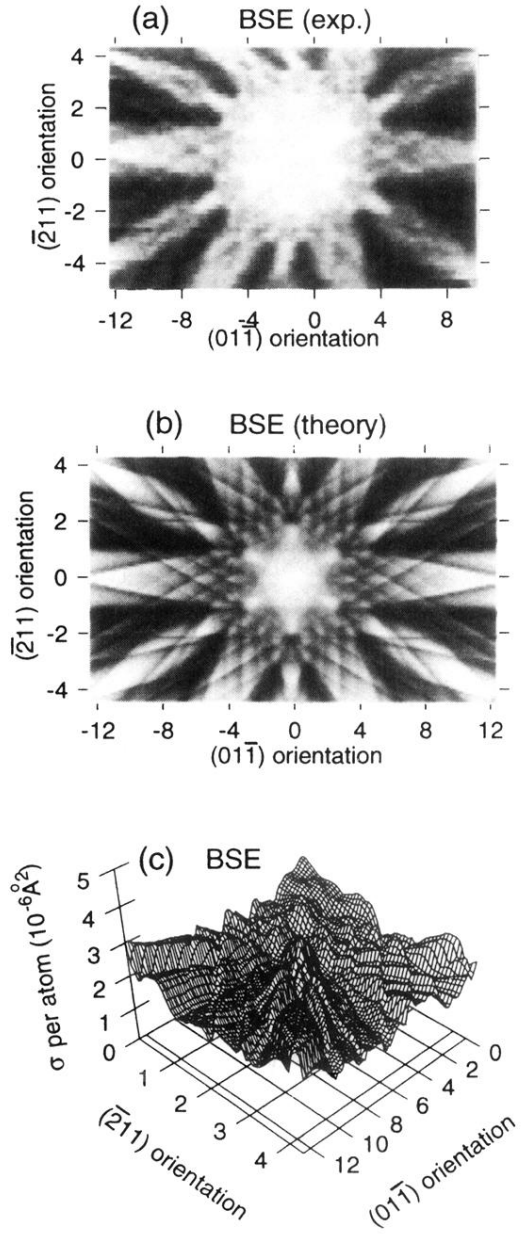


FIG. 12. The backscattered electron cross sections for chromia, as a function of incident beam orientation near the ⟨111⟩ zone axis. (a) experimental results, (b) theoretical results, (c) theoretical results (cross section per atom) as a surface plot. The point (0,0) indicates the beam is in the exact zone-axis orientation, and the $x$ and $y$ scans are in units of the reciprocal lattice vectors $(01\bar{1})$ and $(\bar{2}11)$ respectively.

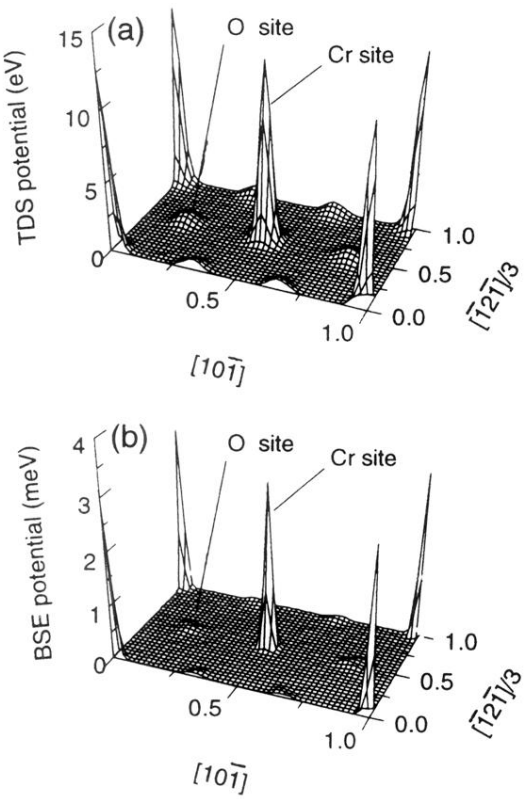


FIG. 13. The projected (along the $\langle 111 \rangle$ zone axis) equivalent local real-space potentials for (a) total thermal diffuse scattering and (b) electron backscattering, in chromia. The potentials are plotted over the region of the unit cell indicated in Fig. 9, and is along the real-space lattice vectors $[10\bar{1}]$ and $[\bar{1}2\bar{1}]/3$. The five largest peaks are due to Cr, and the six smaller peaks are due to O.

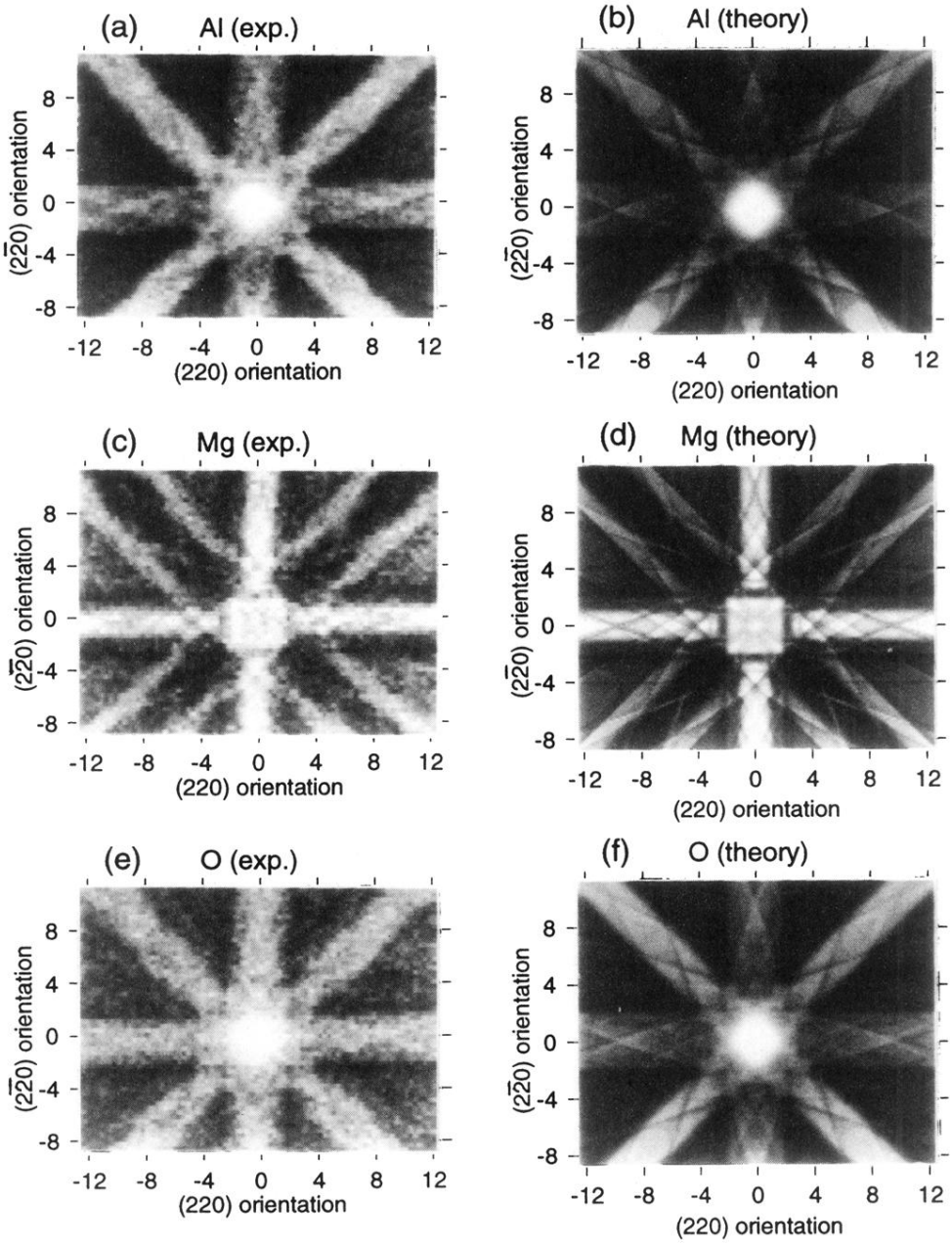


FIG. 3. The $K$-shell ionization cross sections for the constituent atoms of spinel, as a function of orientation of the incident beam near the $\langle 001 \rangle$ zone axis. The $x$ and $y$ coordinates are in units of the reciprocal lattice vectors (220) and (2$\bar{2}$0) respectively. The point (0,0) corresponds to the exact zone axis. (a) Al, experiment; (b) Al, theory; (c) Mg, experiment; (d) Mg, theory; (e) O, experiment; (f) O, theory.

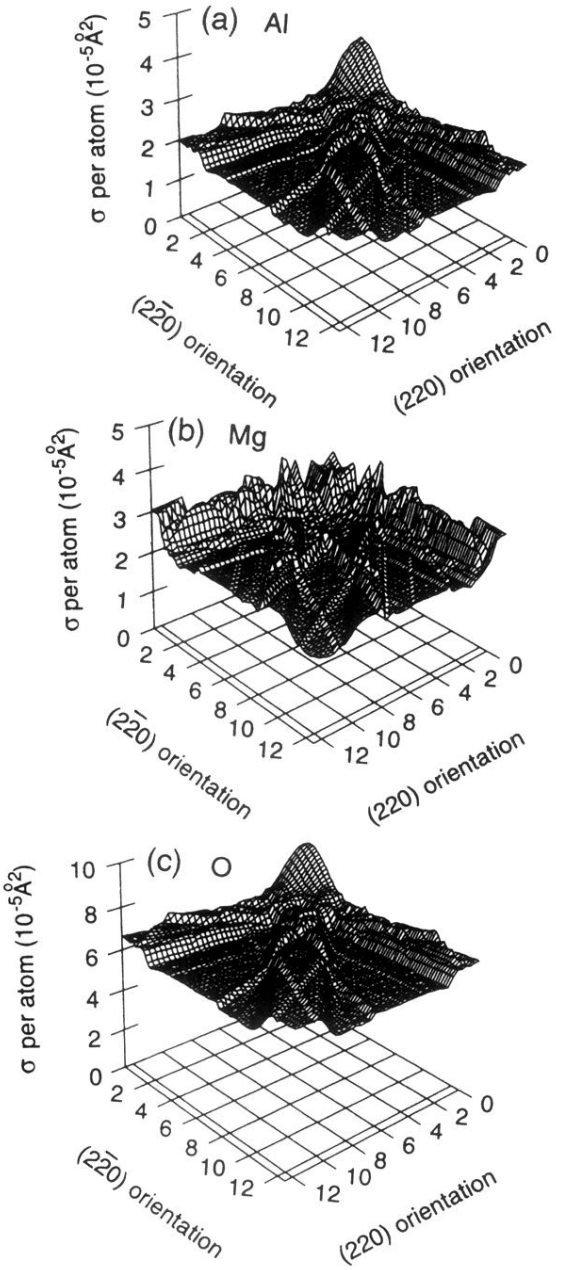


FIG. 4. The calculated $K$-shell ionization cross sections per atom as a surface plot, for the constituent atoms of spinel: (a) Al, (b) Mg, and (c) O. For clarity, only the "first quadrant" of the grey-scale scans in Fig. 3 are shown here.

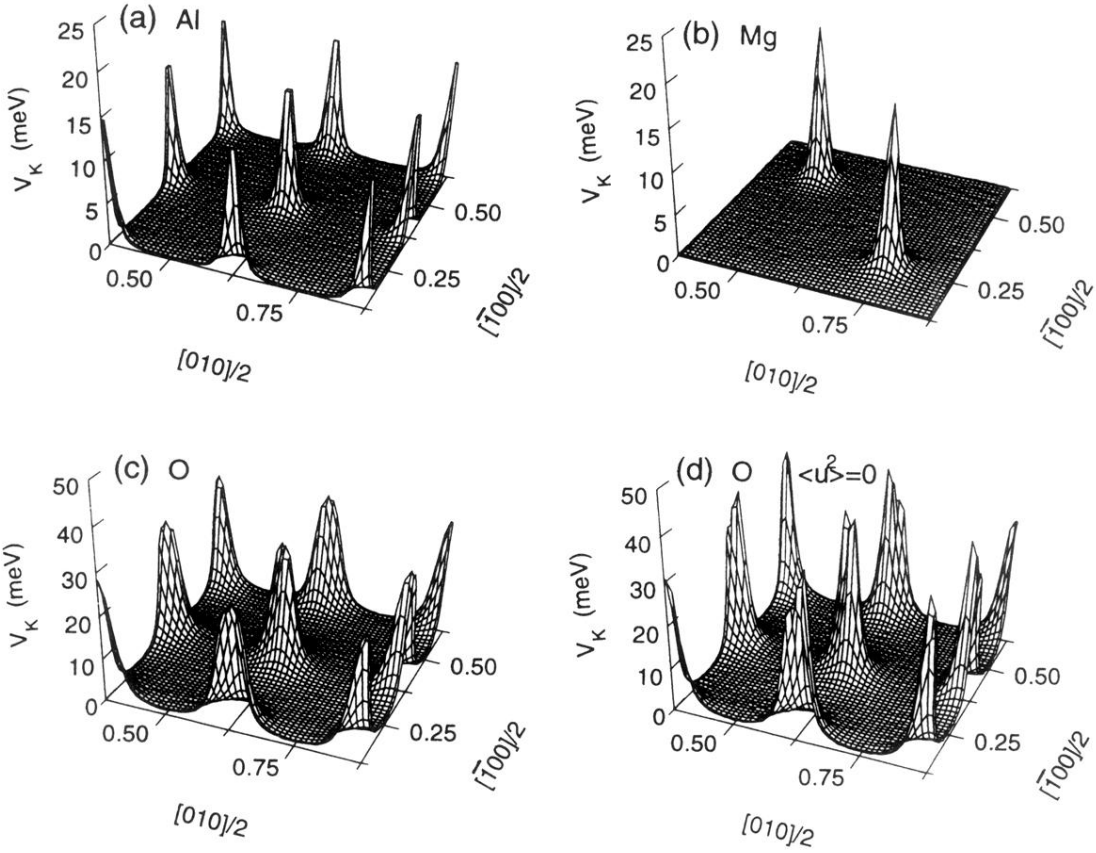


FIG. 5. The projected (along the $\langle 001 \rangle$ zone axis) equivalent local real-space ionization potentials for the constituent atoms of spinel: (a) Al, (b) Mg, (c) O, and (d) O with $\langle u^2 \rangle = 0$. The real-space scan is over the region of the unit cell indicated in Fig. 2, and is along the real-space lattice vectors $[010]/2$ and $[\bar{1}00]/2$.

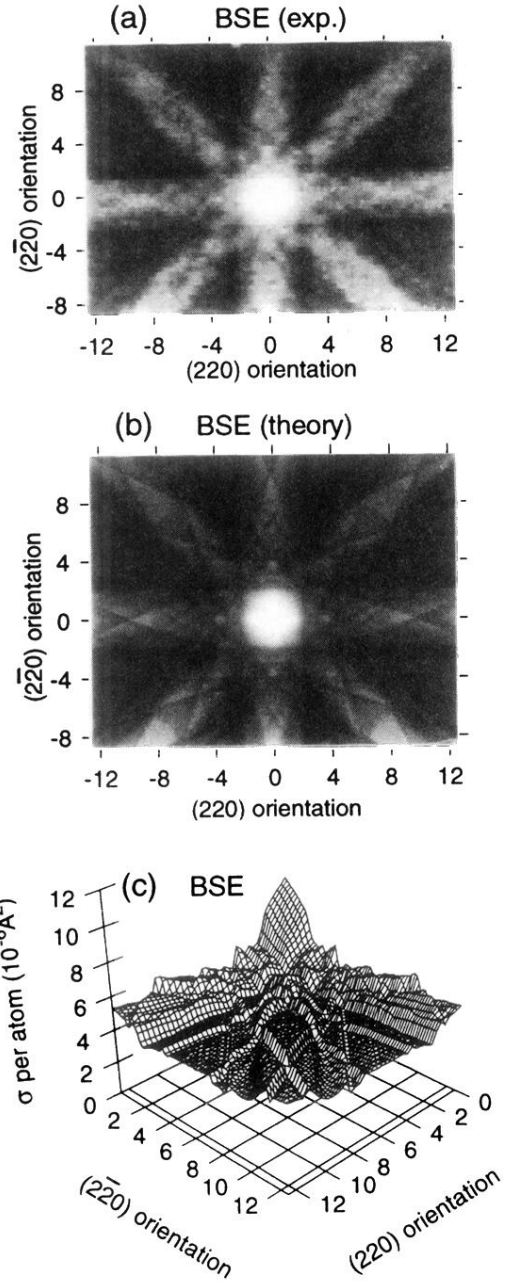


FIG. 6. The backscattered electron cross sections for spinel, as a function of incident beam orientation near the ⟨001⟩ zone axis. (a) experimental results, (b) theoretical results, (c) theoretical results (cross section per atom) on a surface plot. The point (0,0) indicates the beam is in the exact zone-axis orientation, and the $x$ and $y$ scans are in units of the reciprocal lattice vectors (220) and (2$\bar{2}$0) respectively.

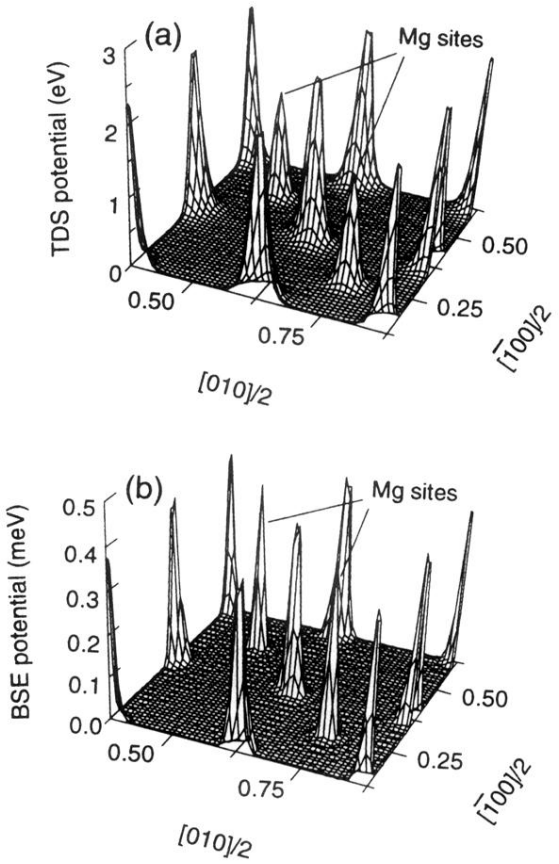


FIG. 7. The projected (along the ⟨001⟩ zone axis) equivalent local real-space potentials for (a) total thermal diffuse scattering and (b) electron backscattering, in spinel. The potentials are plotted for the region of the unit cell indicated in Fig. 2, and is along the real-space lattice vectors [010]/2 and [$\bar{1}$00]/2. The two Mg sites are marked in each figure.